ENERGY DISSIPATION DURING MODE I FRACTURE PROPAGATION IN SHALE: COMPARISON BETWEEN A CONTINUUM DAMAGE MODEL, A COHESIVE ZONE MODEL AND THE EXTENED FINITE ELEMENT METHOD

W. Jin, H. Xu, C. Arson
School of Civil & Environmental Engineering, Georgia Institute of Technology
wencheng.jin@gatech.edu, haoxu@gatech.edu, chloe.arson@ce.gatech.edu

ABSTRACT

We modeled mode I fracture in shale with an equivalent damage zone (CDM), a cohesive zone (CZM) and discontinuous enrichment functions (XFEM). In the Differential Stress Induced Damage model (DSID model) used in the continuum approach the total work input is equal to the sum of the energy released by crack debonding, the energy dissipated by crack opening, and the elastic strain energy stored in the bulk outside of the damage zone. In CZM and XFEM, the overall stiffness of the rock mass in the process zone drops as soon as the fracture starts propagating (unstable fracture propagation), whereas rock elastic properties in the CDM equivalent damage zone evolve smoothly with the displacement imposed at the boundary of the domain. In the CZM and XFEM, fracture propagation stabilizes after a turning point: this point coincides with damage initiation in the DSID model. As a result, the total energy of the rock mass calculated with CDM is about twice as large as in CZM and XFEM. The relative energy components of the rock mass are in the same order of magnitude and follow the same trends in the three models. This numerical study compares the evolution of dissipated energy potentials during mode I fracture propagation, and is expected to provide a basis to predict the amount of energy released by discrete fracture growth vs. damage propagation in the fracture process zone.

KEYWORDS

Bakken shale, mode I fracture propagation, energy dissipation, Finite Element Method, Continuum Damage Mechanics, Cohesive Zone Method, Extended Finite Element Method

INTRODUCTION

In numerical codes, large-scale discontinuities such as hydraulic fractures and faults are usually modeled as separated surfaces or weakly bonded surfaces, or are represented with notch shapes at the macro-scale (Lund, 2007; Adachi et al., 2007). On the contrary, Excavation Damaged Zones are most often modeled with Continuum Damage Mechanics (CDM) models of elasto-plasticity models (Tsang et al., 2005). In Cohesive Zone Models (CZM), fractures propagate along predefined paths, and a governing law (traction-separation law) determines fracture and dissipated energy evolution. In Extended Finite Element Methods (XFEM), the propagation path is not predefined. Discontinuous enrichment functions are added to the shape functions used in standard Finite Element Methods (FEM), in order to account for the presence of fractures (Mohammadi, 2008). CZM and XFEM models are based on fracture mechanics principles: the total energy dissipated during the loading is the energy released to produce new material surfaces within the bulk of the material, and small-scale discontinuities that form the damage process zone around the fracture tip are neglected. Because the initiation and propagation of micro-cracks consume energy, neglecting their effects imply that solid stiffness degradation is neglected, which can lead to under-estimating fracture propagation. At the scale of the Representative Elementary Volume, CDM allows modeling micro-crack propagation with a damage variable that is usually defined as a micro-crack density tensor. An attempt to bridge CDM and fracture mechanics was made by Mazars and Pijaudier-Cabot (1996), who assumed that the energy dissipated prior to large scale fracture instability is solely due to the degradation of elastic properties due to the propagation of micro-cracks in a localized zone, which is fully characterised by a material internal length. Mazars and Pijaudier-Cabot assumed that the internal length

parameter and the energy release rate marking the transition between smeared damage propagation and discrete fracture propagation are known. This energy equivalence is impractical for the prediction of damage and fractures in shale, which is a sedimentary rock with a complex fabric that involves discontinuities at multiple scales. In this paper, we compare three numerical approaches to predict the forms of energy dissipated during mode I fracture propagation in shale. We explain how we calibrated the mechanical model parameters in the first section. The three following sections present the numerical results obtained with the CDM Differential Stress Induced Damage (DSID) model, the CZM and the XFEM, respectively. We compare the evolution of the relative energy components in the last section of the paper.

SHALE CONTINUUM MECHANICS MODEL

In the following, we compare the forms of dissipated energy predicted by three different numerical method during mode I fracture propagation in shale. In the Continuum Damage Mechanics approach, we use the Differential Stress Induced Damage (DSID) model (Xu & Arson, 2014). Table 1 summarizes the main constitutive equations of the DSID model. Stress/strain relationships are derived from the expression of a free energy potential. Damage evolution is controlled by a damage function, similar to Drucker-Prager yield function (but depending on the energy release rate). The damage flow rule is non-associate, and the damage potential is chosen so as to ensure the positivity of dissipation associated to damage. The irreversible deformation due to damage follows an associated flow rule, which allows one to represent physical anisotropic trends of the deformation tensor during the damage process. We calibrated the Continnuum Damage Mechanics parameters of North Dakota Bakken Shale against experimental data obtained during triaxial compression tests performed in the ConocoPhillips rock mechanics laboratory. We optimized the squared residuals of the distance r_i between experimental results y_i and numerical predictions $f(\boldsymbol{x}, \boldsymbol{B})$ as:

$$S = \sum_{i=1}^{n} r_i^2 = \sum_{i=1}^{n} [y_i - f(\boldsymbol{x}, \boldsymbol{B})]^2 \quad (1)$$

Where $\boldsymbol{x}$ is the input known data vector (e.g., strain or stress, depending whether the load is controlled by force or displacement), and $\boldsymbol{B}$ is the vector of unknown parameters that need to be calibrated. We wrote an iterative algorithm in MATLAB to perform the calibration. The first step of the calibration procedure is to give a reasonable initial vector $\boldsymbol{B_0}$ to simulate the triaxial test at the material point using DSID. The gradient method was subsequently employed in order to provide a sequence of $\boldsymbol{B_1}, \boldsymbol{B_2}, \dots, \boldsymbol{B_n}$, as follows:

$$\boldsymbol{B_{n+1}} = \boldsymbol{B_n} - \gamma_n \nabla f(\boldsymbol{x}, \boldsymbol{B}), \quad (2)$$

The algorithm stops when the measure S in Eq. (1) becomes lower than a prescribed value. A set of calibrated DISD parameters for Bakken shale from North Dakota is listed in Table 2.

Table 1. Summary of the constitutive equations of the DSID model

Free energy	$G_s(\sigma, \Omega) = \frac{1}{2}\boldsymbol{\sigma}:\mathbb{S}_0:\boldsymbol{\sigma} + a_1\ \mathrm{Tr}\boldsymbol{\Omega}(Tr\boldsymbol{\sigma})^2 + a_2\ \mathrm{Tr}(\boldsymbol{\sigma}\cdot\boldsymbol{\sigma}\cdot\boldsymbol{\Omega}) + a_3\ \mathrm{Tr}\boldsymbol{\sigma}\ \mathrm{Tr}(\boldsymbol{\Omega}\cdot\boldsymbol{\sigma}) + a_4\ \mathrm{Tr}\boldsymbol{\Omega}\ \mathrm{Tr}(\boldsymbol{\sigma}\cdot\boldsymbol{\sigma})$
	$\epsilon^E = \frac{\partial G_s}{\partial \boldsymbol{\sigma}} = \frac{1+\nu_0}{E_0}\boldsymbol{\sigma} - \frac{\nu_0}{E_0}(\mathrm{Tr}\boldsymbol{\sigma})\boldsymbol{\delta} + 2a_1\ (Tr\boldsymbol{\Omega}Tr\boldsymbol{\sigma})\boldsymbol{\delta} + a_2(\boldsymbol{\sigma}\cdot\boldsymbol{\Omega} + \boldsymbol{\Omega}\cdot\boldsymbol{\sigma}) + a_3\ [Tr(\boldsymbol{\sigma}\cdot\boldsymbol{\Omega})\boldsymbol{\delta} + (\mathrm{Tr}\boldsymbol{\sigma})\boldsymbol{\Omega}] + 2a_4\ (Tr\Omega)\boldsymbol{\sigma}$
	$\boldsymbol{Y} = \frac{\partial G_s}{\partial \boldsymbol{\Omega}} = a_1\ (Tr\boldsymbol{\sigma})^2\boldsymbol{\delta} + a_2\boldsymbol{\sigma}\cdot\boldsymbol{\sigma} + a_3 Tr(\boldsymbol{\sigma})\boldsymbol{\sigma} + a_4\ (\boldsymbol{\sigma}\cdot\boldsymbol{\sigma})\boldsymbol{\delta}$
Damage function	$f_d = \sqrt{J^*} - \alpha I^* - k$
	$J^* = \frac{1}{2}\left(\mathbb{P}_1:\boldsymbol{Y} - \frac{1}{3}I^*\boldsymbol{\delta}\right):\left(\mathbb{P}_1:\boldsymbol{Y} - \frac{1}{3}I^*\boldsymbol{\delta}\right);\ I^* = (\mathbb{P}_1:\boldsymbol{Y}):\boldsymbol{\delta};\ k = C_0 - C_1\mathrm{Tr}(\boldsymbol{\Omega})$
	$\mathbb{P}_1 = \sum_{p=1}^{3}[H(\sigma^p) - H(-\sigma^p)]\boldsymbol{n^p}\otimes\boldsymbol{n^p}\otimes\boldsymbol{n^p}\otimes\boldsymbol{n^p}$

Damage potential	$g_d = \sqrt{\frac{1}{2}(\mathbb{P}_2 : \boldsymbol{Y}) : (\mathbb{P}_2 : \boldsymbol{Y})}$ $\mathbb{P}_2 = \sum_{p=1}^{3} H\left[\max_{p=1}^{3} \sigma^p - \sigma^p\right] \boldsymbol{n^p} \otimes \boldsymbol{n^p} \otimes \boldsymbol{n^p} \otimes \boldsymbol{n^p}$
Flow rule	$\dot{\epsilon}^{id} = \dot{\lambda}_d \frac{\partial f_d}{\partial \boldsymbol{\sigma}} = \dot{\lambda}_d \frac{\partial f_d}{\partial \boldsymbol{Y}} \frac{\partial \boldsymbol{Y}}{\partial \boldsymbol{\sigma}}$ $\dot{\boldsymbol{\Omega}} = \dot{\lambda}_d \frac{\partial g_d}{\partial \boldsymbol{Y}}$

G_s: Gibbs free energy	$\boldsymbol{\sigma}$: Stress tensor	$\mathbb{S}_0$: Undamaged compliance tensor
ϵ^E: Total elastic strain	ν_0: Poisson's ratio	$\boldsymbol{Y}$: Damage driving force
E_0: Young's Modulus	$\boldsymbol{\delta}$: Kronecker delta	C_0: Initial damage threshold
$\mathbb{P}_1, \mathbb{P}_2$: Projection tensors	H: Heaviside function	a_1, a_2, a_3, a_4: Material parameters
$\dot{\epsilon}^{id}$: Irreversible strain rate	$\dot{\lambda}_d$: Lagrangian Multiplier	C_1: Damage hardening variable
$\dot{\boldsymbol{\Omega}}$: Damage rate	$\boldsymbol{\Omega}$: Damage variable	$\sigma^p, \boldsymbol{n^p}$: Principal stress and corresponding direction

Table 2: Calibrated DSID parameters for Bakken shale

Elasticity		Free energy				Damage function		
E	ν	a_1	a_2	a_3	a_4	C_0	C_1	α
GPa	-	GPa^{-1}	GPa^{-1}	GPa^{-1}	GPa^{-1}	MPa	MPa	-
46	0.186	7.35×10^{-4}	0.121	-3.15×10^{-2}	2.39×10^{-3}	0.01	1.18	0.399

GEOMETRY AND BOUNDARY CONDITIONS OF THE NUMERICAL MODELS

The geometry of the 3D domain studied in the following is shown in Fig.1. In all the simulations, horizontal displacements are fixed along the vertical boundaries. Vertical displacements are imposed on part of the top and bottom boundaries. An initial small crack is embedded at mid-height of the domain, on the left-hand side. We anticipate that displacements will open the initial crack and induce stress concentrations around the crack tip, which will cause damage propagation (with the DSID model) or crack propagation in the x-direction (with the CZM and the XFEM).

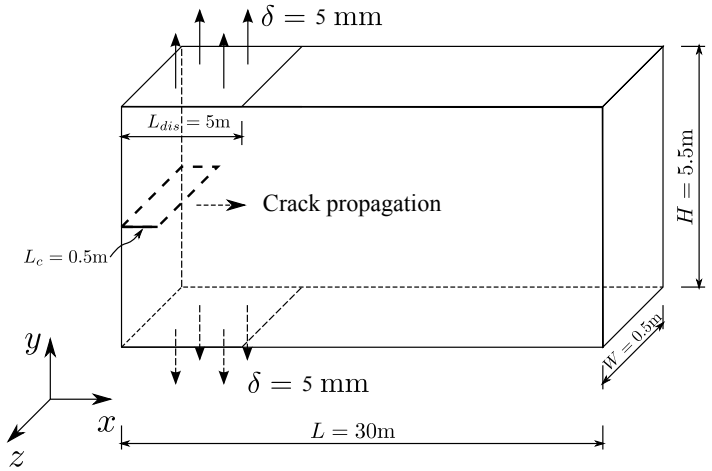

Figure 1. Geometry and boundary conditions adopted in the numerical models.

ENERGY DISSIPATED AROUND A MODE I FRACTURE WITH THE DSID MODEL

We first use the Finite Element Method (FEM) to simulate the propagation of anisotropic damage in mode I. The energy dissipated during the displacement loading is derived from the Inequality of Clausius-Duhem:

$$\dot{\Phi}_s = \boldsymbol{\sigma}:\dot{\boldsymbol{\epsilon}} - \dot{\psi}_s = \boldsymbol{\sigma}:\dot{\boldsymbol{\epsilon}}^{id} + \boldsymbol{Y}:\dot{\boldsymbol{\Omega}} \geq 0 \tag{3}$$

In which $\dot{\boldsymbol{\Phi}}_{\boldsymbol{s}}$ is the dissipated energy for each load step. The work done by external forces is $\boldsymbol{\sigma}:\dot{\boldsymbol{\epsilon}}$ at each loading step, so at the end of the simulation, the total work done is $\int \boldsymbol{\sigma}:\dot{\boldsymbol{\epsilon}}\boldsymbol{dt}$. The total elastic strain energy stored in the solid bulk is $\frac{1}{2}\boldsymbol{\sigma}:\dot{\boldsymbol{\epsilon}}^{E}$. The dissipated energy, $\int \dot{\Phi}_s \mathrm{d}t$, is the difference between the external work and the recoverable strain energy. The energy lost during the loading should always be non-negative:

$$\int \dot{\Phi}_s \mathrm{d}t = \int \boldsymbol{\sigma}:\dot{\boldsymbol{\epsilon}}\mathrm{d}t - \frac{1}{2}\boldsymbol{\sigma}:\dot{\boldsymbol{\epsilon}}^{E} = \int \boldsymbol{\sigma}:\dot{\boldsymbol{\epsilon}}^{id}\mathrm{d}t + \int \boldsymbol{Y}:\dot{\boldsymbol{\Omega}}\mathrm{d}t \geq 0 \tag{4}$$

The energy dissipated by damage consists of two parts: the energy released to debond bulk material surfaces without additional deformation (denoted $\int \boldsymbol{Y}:\dot{\boldsymbol{\Omega}}\mathrm{d}t$), and the energy dissipated to produce irreversible bulk deformation when crack faces open (denoted $\int \boldsymbol{\sigma}:\dot{\boldsymbol{\epsilon}}^{id}\mathrm{d}t$). We do not account for non-mechanical energy transfer (such thermal transport or radiation). Fig.2 illustrates the decomposition of the energy spent during the loading process, including the two forms of energy dissipated and the elastic strain energy stored in the bulk. Note that damage propagation reduces material stiffness, which increases the capacity of the material to store deformation energy. Energy conservation is written as:

$$\int \boldsymbol{\sigma}:\dot{\boldsymbol{\epsilon}}\mathrm{d}t = \int \boldsymbol{\sigma}:\dot{\boldsymbol{\epsilon}}^{el}\mathrm{d}t + \frac{1}{2}\boldsymbol{\sigma}:\dot{\boldsymbol{\epsilon}}^{ed} + \int \boldsymbol{\sigma}:\dot{\boldsymbol{\epsilon}}^{id}\mathrm{d}t + \int \boldsymbol{Y}:\dot{\boldsymbol{\Omega}}\mathrm{d}t \tag{5}$$

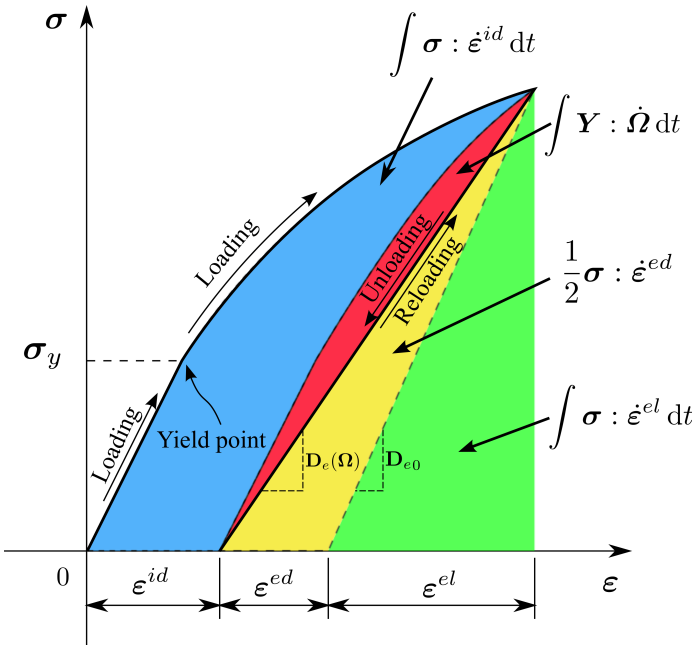

Figure 2: Decomposition of the energy spent during the loading process in the DSID model.

In order to compare the results obtained with the Finite Element CDM model with predictions made with the CZM and the XFEM approaches, we assume that damage will concentrate in a narrow horizontal band ahead of the tip of the initial defect. By this means, energy can only dissipate in the zone where a discrete fracture is expected to propagate. The DSID model is assigned to the two central Finite Elements at mid-height of the domain. Above and below this central band, we adopt a linear elastic model, in which the Young's modulus and the Poisson's ratio are the ones indicated in Table 2.

Fig.3 shows the evolution of the three energy components with the displacements imposed at the top and bottom of the domain. No discontinuity is observed in the plots, which indicates that damage

propagation was stable. For displacements inferior to one millimeter, the total energy was equal to the elastic energy component, due to the absence of damage. After that threshold, damage propagated. The dissipation of energy for crack debonding was of the same order of magnitude as for irreversible deformation. Note that the elastic strain energy stored in the bulk kept increasing after the initiation of damage (whereas in fracture mechanics approaches, the elastic strain energy storage rate goes to zero during mode I fracture propagation).

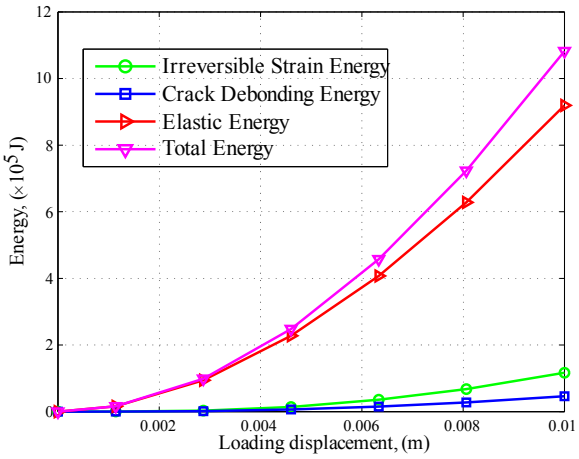

(a) Evolution of the energy components

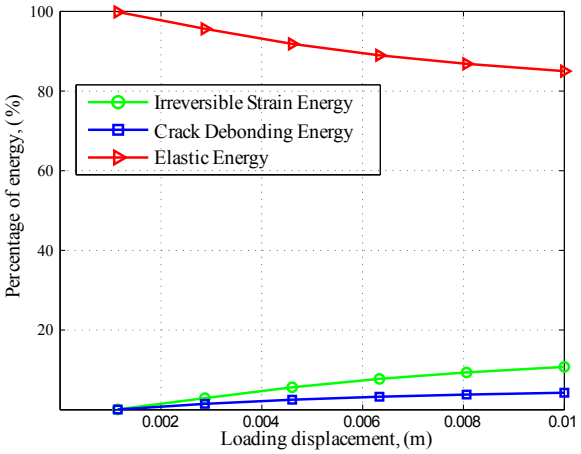

(b) Evolution of the relative energy components

Figure 3: Forms of energy dissipated in mode I with the DSID model

ENERGY DISSIPATED AROUND A MODE I FRACTURE WITH A CZM MODEL

In the cohesive-zone models, a stress displacement relationship across the crack tip represents the degrading mechanisms that occur in the fracture process zone. Fig.4 illustrates the principle of the quasi-brittle fracture model employed in the following simulations. The cohesive crack tip corresponds to the damage initiation point where the traction reaches the cohesive strength σ_{max} and the separation reaches the critical value δ_0; the material crack tip is the complete failure point where the separation reaches the critical value δ_f and the traction or cohesive strength acting across the surfaces are equal to zero. The mechanical work needed to create a unit area of fully debonded crack is referred to as the fracture energy (noted G_c). According to Gurtin's thermodynamic study of the cohesive method (Gurtin, 1979), the energy release rate for a sharp crack surrounded by a homogeneous hyper-elastic body is

$$G_c = \int \sigma d\delta. \tag{6}$$

The displacement threshold for damage initiation and the extent of the damage process zone predicted under given loading conditions depend on the cohesive law employed in the numerical model. However, the value of the energy release rate G_c is an intrinsic material property that can be directly related to fracture toughness K_c in linear elastic fracture mechanics as

$$G_c = \frac{K_{IC}^2}{E'} + \frac{K_{IIC}^2}{E'} + \frac{K_{IIIC}^2}{2G}. \quad (7)$$

Where $E' = E$ in plain stress and $E' = E/(1-\nu^2)$ in plane strain.

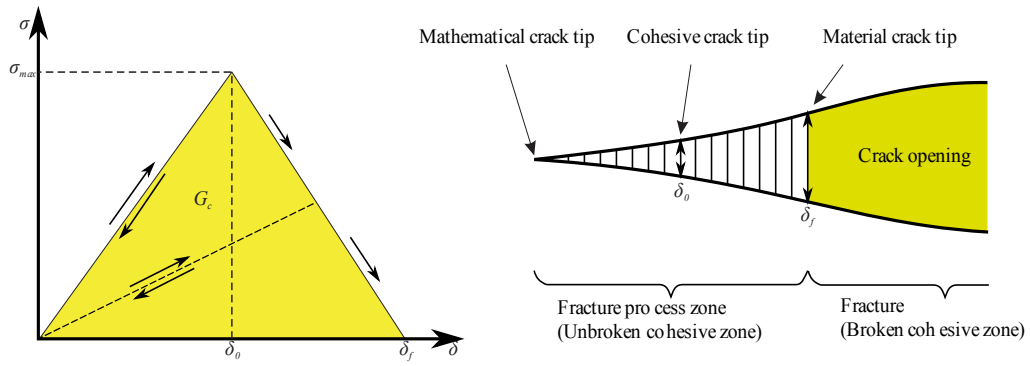

(a) (b)

Figure 4. (a) Bilinear cohesive law employed in the quasi-brittle fracture model. (b) Traction-displacement sketch characterizing the cohesive zone

In order to calibrate the value of G_c for North Dakota Bakken Shale, we assume that the energy dissipated for continuum damage initiation in the two elements ahead of the initial tip equals the energy necessary to split two CZM elements:

$$\int \dot{\Phi}_d dt = \int \boldsymbol{\sigma}: \dot{\boldsymbol{\epsilon}}^{id} \mathrm{d}t + \int \boldsymbol{Y}: \dot{\boldsymbol{\Omega}} \mathrm{d}t = \int G_c \dot{A} dt. \quad (6)$$

After numerical calculations, we obtained G_c=20N/m. The maximum nominal stress σ_{max} was determined experimentally in the ConocoPhillips rock mechanics laboratory for Bakken Shale: we took an average value of 8MPa. Before damage initiation, we used the undamaged Young's modulus to calculate the slope of the stress displacement relationship used in the numerical CZM contact model.

Fig.5 shows the evolution of the elastic strain energy stored in the bulk and the irreversible strain energy dissipated with the displacements imposed at the top and bottom of the domain. The irreversible strain energy was calculated as the product of the fracture surface and the energy release rate G_c. The elastic strain energy was automatically calculated by the Finite Element program in the elastic domain. The magnitudes of the energy components (Fig.5) are about half of those obtained with the DSID model (Fig.3). This difference can be explained by the dramatic drop of stiffness of the overall domain when the cohesive zone propagates. In the CZM simulations, the elastic energy stored in the domain and the irreversible energy dissipated to form fracture surfaces increase abruptly for displacement inferior to one millimeter. However, the percentage of elastic energy to the total energy decreases at the occurrence of the crack propagation, while the percentage of energy dissipated increases. After this stage, fracture propagation is stable: elastic and irreversible energy components increase, but the percentage of both elastic and irreversible energy components remain the same throughout the simulation.

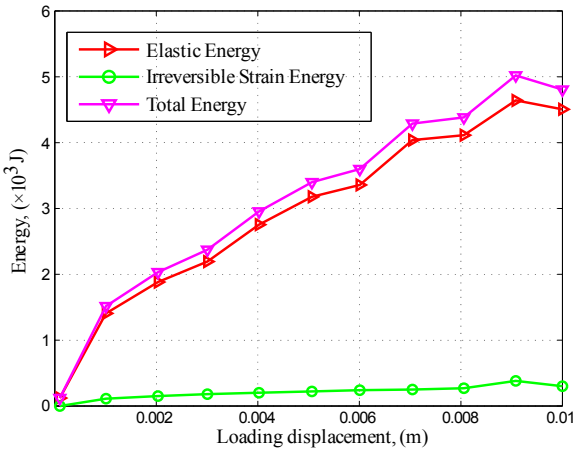

(a) Evolution of the energy components

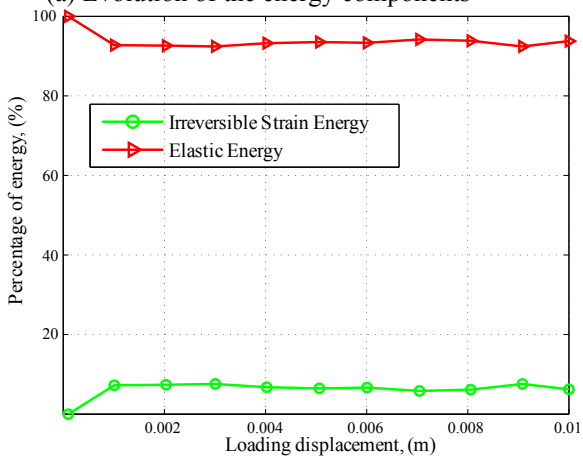

(b) Evolution of the relative energy components

Figure 5: Forms of energy dissipated in mode I with the CZM model

ENERGY DISSIPATED AROUND A MODE I FRACTURE WITH A XFEM MODEL

The idea sustaining XFEM is to add discontinuous enrichment functions to the Finite Element approximation, in order to account for the presence of the crack. The geometry of the cracks is explicitly modeled and finer remeshing is not required. The enrichment functions typically consist of near-tip asymptotic functions that capture the singularity around the crack tip and a discontinuous function that represents the jump in displacement across the crack surfaces:

$$\mathbf{u} = \sum_{i=1}^{n} N_i(\boldsymbol{x})[\boldsymbol{u_i} + H(x)\boldsymbol{a_i} + \sum_{\alpha=1}^{4} F_\alpha(x)\boldsymbol{b_i^\alpha}] \quad (8)$$

Where $N_i(x)$ are the usual nodal shape functions; $\boldsymbol{u_i}$ is the usual nodal displacement vector associated with the continuous part of the finite element solution; the second term is the product of the nodal enriched degree of freedom vector $\boldsymbol{a_i}$ with the associated discontinuous jump function $H(x)$ across the crack surfaces; and the third term is the product of the nodal enriched degree of freedom vector, $\boldsymbol{b_i^\alpha}$ and the associated elastic asymptotic crack-tip functions $F_\alpha(x)$. We use a XFEM model based on the so-called cohesive theory. Fig.6 illustrates the principle of the traction-displacement law adopted in the following simulations.

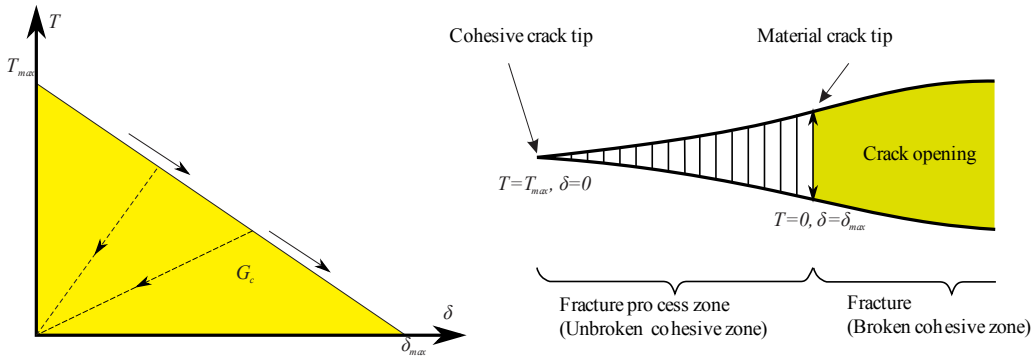

Figure 6. XFEM model based on the linear cohesive theory

Similar to the CZM model, we use a critical energy release rate G_c equal to 20N/m. The maximum traction force divided by fractured area $\frac{T_{max}}{2dA}$ is set as 8MPa in XFEM modeling. Energy components are calculated in the same way as in the CZM model presented above. Fig.7 shows the evolution of the elastic strain energy stored in the bulk and the irreversible strain energy dissipated with the displacements imposed at the top and bottom of the domain. The comparison of Fig.5 and Fig.7 sows that XFEM predictions match CZM prediction with a relative difference of less than 5%. The maximum accumulated elastic energy is slightly larger in XFEM than in CZM.

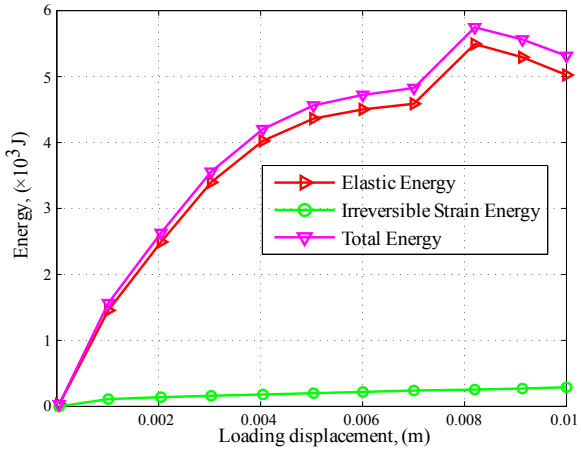

(a) Evolution of the energy components

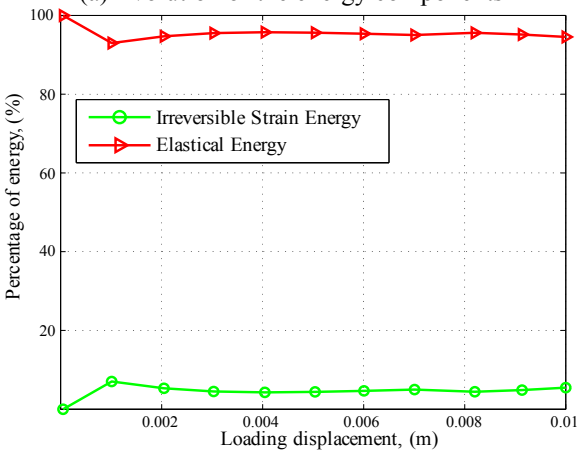

(b) Evolution of the relative energy components

Figure 5: Forms of energy dissipated in mode I with the XFEM model

DISCUSSION

In order to compare the forms of energy dissipated as predicted by the CDM, CZM and XFEM approaches, we plotted the evolution of the percentage of the elastic energy within the entire study domain and the percentage of dissipated energy from damage evolution and fracture propagation (Fig.8). Both XFEM and CZM account for the generation of a discontinuity therefore the percentage of the elastic energy reduces rapidly when the mode I fracture starts to propagate. As the energy percentage reaches a turning point, the crack extension slows down and becomes stable. The percentage of elastic and irreversible to total energy have nearly constant values after the turning point. However, this phenomenon cannot be captured with CDM: damage propagation in the DSID model represents the growth of a fractured zone equivalently represented by a crack density tensor. Even though the discontinuity is not represented explicitly, the advantage of CDM is that it avoids instabilities: energy components evolve smoothly with the displacements imposed at the top and bottom of the domain.

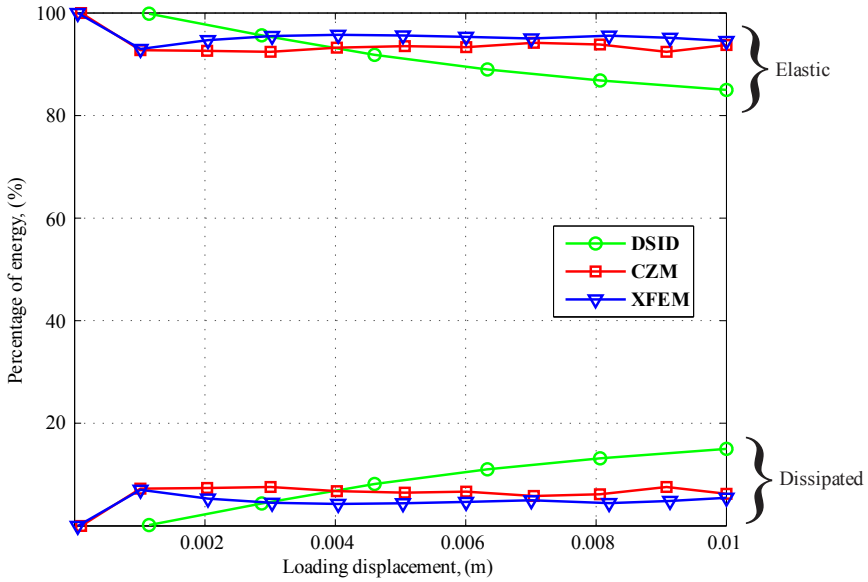

Figure 8. Evolution of the relative energy components in mode I with the DSID, CZM and XFEM models.

CONCLUSION

We modeled mode I fracture in shale with an equivalent damage zone (CDM), a cohesive zone (CZM) and discontinuous enrichment functions (XFEM). The Differential Stress Induced Damage model (DSID model) used in the continuum approach allows one to predict the energy released by micro-crack debonding the irreversible strain energy dissipated by micro-crack opening. The width and extent of the equivalent damage zone representing the fracture are pre-assigned in the model. The total work input is equal to the sum of the energy released by crack debonding, the energy dissipated by crack opening, and the elastic strain energy stored in the bulk outside of the damage zone. In CZM and XFEM, mode I propagation is governed by fracture mechanics principles and the total work input is equal to the energy released by fracture propagation plus the elastic strain energy stored in the bulk. In contrast to CZM, XFEM models do not require pre-assigning the fracture path. In CZM and XFEM, the overall stiffness of the rock mass in the process zone drops as soon as the fracture starts propagating (unstable fracture propagation), whereas rock elastic properties in the CDM equivalent damage zone evolve smoothly with the displacement imposed at the boundary of the domain. In CZM and XFEM, fracture propagation stabilizes after a turning point: this point coincides with damage initiation in the DSID model. As a result, the total energy of the rock mass calculated with CDM is about twice as large as in CZM and XFEM. The

relative energy components of the rock mass are of the same order of magnitude and follow the same trends in the three models. The continuum mechanics approach avoids unstable fracture propagation and allows one to predict different forms of energy dissipation in the fracture process zone. Coupling the CDM approach with fracture mechanics numerical models (such as the CZM or the XFEM) would allow one to predict the coupled propagation of a discrete fracture and its process zone. Former studies were based on equivalent energy thresholds to predict the transition between smeared damage propagation and discrete fracture propagation, and required the introduction of internal material lengths to predict the extent of the damaged zone. This numerical study compares the evolution of dissipated energy potentials during mode I fracture propagation, and is expected to provide a basis to predict the amount of energy released by discrete fracture growth vs. damage propagation in the fracture process zone. The main applications of this research are fault mechanics and hydraulic fracture propagation – especially in shale, in which there is no clear evidence of what the internal length should be.

ACKNOWLEDGEMENTS

The authors are thankful to their research sponsors: Georgia Tech School of Civil and Environmental Engineering, Georgia Tech Offices of the Provost and Executive Vice President for Research, and ConocoPhillips.

REFERENCES

Adachi, J., Siebrits, E., Peirce, A., & Desroches, J. (2007). Computer simulation of hydraulic fractures. International Journal of Rock Mechanics and Mining Sciences, 44(5), 739-757.

Gurtin, M. E. (1979). Thermodynamics and the cohesive zone in fracture. Zeitschrift für angewandte Mathematik und Physik ZAMP, 30(6), 991-1003.

Halm, D., & Dragon, A. (1998). An anisotropic model of damage and frictional sliding for brittle materials. European Journal of Mechanics-A/Solids, 17(3), 439-460.

Lund, J. W. (2007). Characteristics, development and utilization of geothermal resources. GHC Bulletin, 28(2), 1-9.

Mazars, J., & Pijaudier-Cabot, G. (1996). From damage to fracture mechanics and conversely: a combined approach. International Journal of Solids and Structures, 33(20), 3327-3342.

Mohammadi, S. (2008). Extended finite element method: for fracture analysis of structures. John Wiley & Sons.

Shao, J. F., Zhou, H., & Chau, K. T. (2005). Coupling between anisotropic damage and permeability variation in brittle rocks. International Journal for Numerical and Analytical Methods in Geomechanics, 29(12), 1231-1247.

Tsang, C. F., Bernier, F., & Davies, C. (2005). Gepohydromechanical processes in the Excavation Damaged Zone in crystalline rock, rock salt, and indurated and plastic clays—in the context of radioactive waste disposal. International Journal of Rock Mechanics and Mining Sciences, 42(1), 109-125.

Xu, H., & Arson, C. (2014). Anisotropic Damage Models for Geomaterials: Theoretical and Numerical Challenges. International Journal of Computational Methods, 11(02).